MATERIALS CHEMISTRY
FRONTIERS

RESEARCH ARTICLE

View Article Online
View Journal | View Issue

Cite this: *Mater. Chem. Front.*, 2022, **6**, 956

A DNA functionalized metal–organic framework combined with magnesium peroxide nanoparticles: targeted and enhanced photodynamic therapy†

Xinran Sun, Guoda Zhang, Xilai Ding, Yingyan Liu, Kaixiu Chen, Pengfei Shi* and Shusheng Zhang *

Received 3rd November 2021,
Accepted 22nd February 2022

DOI: 10.1039/d1qm01475g

rsc.li/frontiers-materials

Photodynamic therapy (PDT) has become a promising therapeutic approach in clinical practices. How to improve the efficiency of PDT is still a research hotspot due to tumor hypoxia and insufficient aggregation of photosensitizers (PSs) at the tumor site. Here, we report an aptamer functionalized metal–organic framework combined with magnesium peroxide nanoparticles (Hf-MOF-MgO_2/DNA) to target and enhance PDT. Hf-MOF-MgO_2/DNA could produce oxygen in sufficient quantities, solving the hypoxia problem and enhancing PDT. The aptamer simultaneously and specifically targets tumor cells, performing targeted therapy. After PDT treatment *in vitro*, the Hf-MOF-MgO_2/DNA platform functionalized by the aptamer of 4T1 cells specifically targeted the cell and achieved a survival rate of 15.15% for the 4T1 cell, while the survival rate for the A549 cell was 28.69% under the same conditions. This work highlights a rational design for efficient reactive oxygen generation *in situ* and effective PS accumulation in tumors, opening new horizons for the development of theranostic nanomedicines.

Introduction

Photodynamic therapy is rapidly developing as an effective therapeutic approach against tumors in virtue of being non-invasive, high selectivity and minimum side effects.[1–3] An effectively accumulated photosensitizer (PS) in tumors absorbs the light of a specific wavelength, followed by transferring the energy to the surrounding oxygen molecules, which further produces cytotoxic reactive oxygen species (ROS).[4,5] In addition to directly leading to apoptosis and/or necrosis, high levels of ROS in the cell could also induce shut down of the tumor vasculature and activation of the immune system.[6–8] By localizing both the PS and the light exposure to tumor regions, PDT can precisely kill tumor cells without causing damage to the surrounding normal tissue.[9–11] As a result, PDT is currently being used to treat head and neck cancer, pancreatic cancer, and mesothelioma in clinical practices.[12] With the investigation on PDT treatment progressing, it is imperative to develop more effective methods to improve the PDT efficiency.[13] When seeking to improve PDT, the design and synthesis of the PS, the control and transmission of light and increasing the production of O_2 are the key directions.[14–16] The first PS appeared with the discovery of hematoporphyrin (HP) and the clinical application of its derivatives (HPDs) in the early 1980s.[17] However, poor tumor selectivity, relatively poor tissue penetration, strong and lasting skin photosensitivity, poor light absorption and poor aqueous solubility or dispersity made the previous PS unideal for PDT.[18] The emergence and development of nanotechnology obviously provide great potential for the renewal of the PS, which surmount solubility and aggregation issues, improve the aggregation of the PS in tumors and eliminate organic hydrotropes. In 2014, Lin's group first reported Hf-based nanoscale metal–organic frameworks (nMOFs) with porphyrins as ligands, providing a new strategy for PDT.[19] The PS can be regularly introduced into nMOFs by linking to metal nodes.[20] This strategy prevents the aggregation or self-quenching of the PS in aqueous solutions, achieving a high PS loading capacity. Furthermore, the excellent biocompatibility and biodegradability also make it possible for MOFs to become the desired PS.[21]

With the promising development of nanotechnology, the therapeutic efficiency of PDT is severely limited by tumor hypoxia.[22] The uncontrolled growth of tumor cells and the abnormal formation of tumor blood vessels result in insufficient oxygen supply. In addition, microvascular collapse caused by PDT inevitably aggravates the hypoxia conditions, seriously

Shandong Provincial Key Laboratory of Detection Technology for Tumor Markers, School of Chemistry and Chemical Engineering, Linyi University, Linyi 276000, Shandong, P. R. China. E-mail: shipengfei913@163.com, shushzhang@126.com

† Electronic supplementary information (ESI) available: XPS, TEM, PXRD, DCFH fluorescence, UV-vis, CLSM, images of O_2 bubbles, tumor weight, and fluorescence imaging of mice and organs. See DOI: 10.1039/d1qm01475g

restricting the PDT efficiency.[23,24] In recent years, a large number of nMOF based nanoplatforms exhibiting catalytic activity or self-generating reactive oxygen species were applied to enhance the PDT efficiency.[25–27] For example, Min's group constructed a nanoplatform named aMMTm, in which MnO_2 coated on PCN nMOFs could remove GSH from tumors, reduce ROS consumption and improve the PDT efficiency.[28] Gao's group also designed and synthesized two-dimensional nMOFs for the *in situ* growth of platinum nanozymes to obtain adequate oxygen supply during PDT.[29] Liu's group used PCN to simultaneously embed glucose oxidase-mimicking ultrasmall gold nanoparticles (Au NPs) and catalase-mimicking platinum nanoparticles (Pt NPs) to promote the catalysis of H_2O_2 and produce O_2.[30] More recently, Bu designed transferrin-modified magnesium peroxide (MgO_2) nanoparticles for delivering ROS to cancer cells.[31] MgO_2 is an oxygen-releasing compound, which is slowly decomposed into H_2O_2 when it comes in contact with water and further converted into O_2.[32,33] Thus, MgO_2 is expected to become an oxygen-producing material for tumor therapy due to its good biocompatibility and oxygen release capacity. In addition to the efficient production of ROS, it is also important to selectively accumulate the PS in tumors to minimize the damage to the healthy tissue. The targeted therapy is optimal to minimize the damage to the healthy tissue and enhance the curative effect.[34,35] Although PDT can induce tumor cell apoptosis by accurately immobilizing the laser, the accumulation of the nanosystem in tumors depends on tumor angiogenesis and regeneration, which makes accumulation in tumors ineffective by passive targeting alone. Therefore, many studies have focused on introducing active targeting elements into nanosystems that can specifically bind to the receptors on the surface of tumor cells. The targeted groups usually include folic acid (FA),[36] hyaluronic acid (HA),[37,38] aptamers,[39] targeted peptides[40] and epidermal growth factor receptor-bound adjuncts.[41]

Herein, we reported a simple strategy for enhanced and targeted PDT by decorating magnesium peroxide nanoparticles and a specific aptamer of tumor cells on MOFs. As shown in Scheme 1, Hf-MOF nanoparticles, isomorphic to PCN-224, were synthesized. Then, Hf-MOF-MgO_2 was obtained by the *in situ* growth of MgO_2 nanoparticles with the Hf-MOF. The aptamer (DNA) of the breast cancer cell line 4T1 was also modified on Hf-MOF-MgO_2 by Hf–O coordinated interactions to obtain Hf-MOF-MgO_2/DNA. The O_2 produced by MgO_2 could readily release and solve the oxygen deficiency, further improving the efficacy of PDT. Moreover, the aptamer targeted specifically to the 4T1 cells, realizing targeted therapy. Under 650 nm light irradiation at a power density of 0.28 W cm^{-2}, significantly targeting and enhancing PDT mediated by Hf-MOF-MgO_2/DNA was achieved both *in vitro* and *in vivo*.

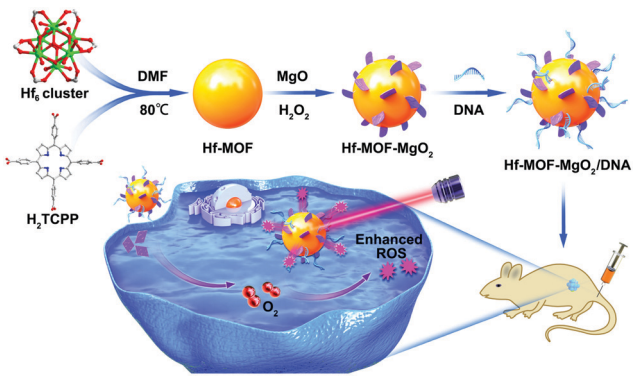

Scheme 1 Schematic representation of magnesium peroxide nanoparticles and the aptamer decorated MOF for enhanced photodynamic therapy.

Results and discussion

The nanocomposite Hf-MOF-MgO_2/DNA was synthesized by *in situ* growth and post-modification. First, the Hf-MOF was prepared using a solvothermal method by heating equal molar amounts of $HfCl_4$ and H_2TCPP in *N*,*N*′-dimethylformamide (DMF) at 80 °C for 24 h. Second, MgO_2 was grown on the surface of the Hf-MOF using a microemulsion-like method to form Hf-MOF-MgO_2. Finally, the aptamer (DNA) of the breast cancer cell 4T1 was modified on Hf-MOF-MgO_2 by strong coordination interactions between the phosphate group and Hf^{4+} ions, forming Hf-MOF-MgO_2/DNA. The morphologies of the obtained Hf-MOF and Hf-MOF-MgO_2/DNA were observed by transmission electron microscopy (TEM). Fig. 1a and b show that the Hf-MOF was characterized by a good monodispersed size distribution of approximately 200 nm. After composition with MgO_2 and DNA, the diameter of the Hf-MOF became larger but the morphology remained unchanged. MgO_2 nanoparticles were attached to the surface of the Hf-MOF. HRTEM clearly demonstrated the lattice fringe with an interplanar spacing of 0.252 nm (Fig. 1c), related to the (200) plane of MgO_2.[42] In addition, TEM elemental mapping (Fig. 1d) and energy dispersive spectra (Fig. 1e) showed the homogeneous distribution of Hf, Mg, C, N, O and P elements in the same particle, demonstrating the decoration of MgO_2 NPs and DNA on the Hf-MOF. X-ray photoelectron spectroscopy (XPS) was further performed to understand the elements and the valence state, as shown in Fig. 1f and Fig. S1–S3 (in the ESI†).

The binding energies of the elements Hf and Mg were 18.5 eV and 1304.3 eV, respectively. The lower valence state of O (O_2^{2-}) in XPS was indistinguishable due to the presence of carboxyl groups in TCPP. Additionally, pure MgO_2 nanoparticles were prepared using the microemulsion-like method in the absence of the Hf-MOF. The as-prepared MgO_2 (Fig. S4) showed a similar morphology to that in Hf-MOF-MgO_2/DNA. The powder X-ray diffraction (PXRD) patterns of MgO_2 revealed the presence of distinct peaks (2θ) at 37.0°, 53.7°, and 62.4° referred to the 200, 220 and 311 facets of MgO_2, respectively, according to the values reported in the literature for MgO_2 (JCPDS 76-1363), as shown in Fig. S5 (ESI†). The typical diffraction peaks referred to MgO_2 in Hf-MOF-MgO_2/DNA were not clear, which may be ascribed to the low crystallinity of MgO_2 and be masked by large diffraction peaks of the Hf-MOF.[43] The

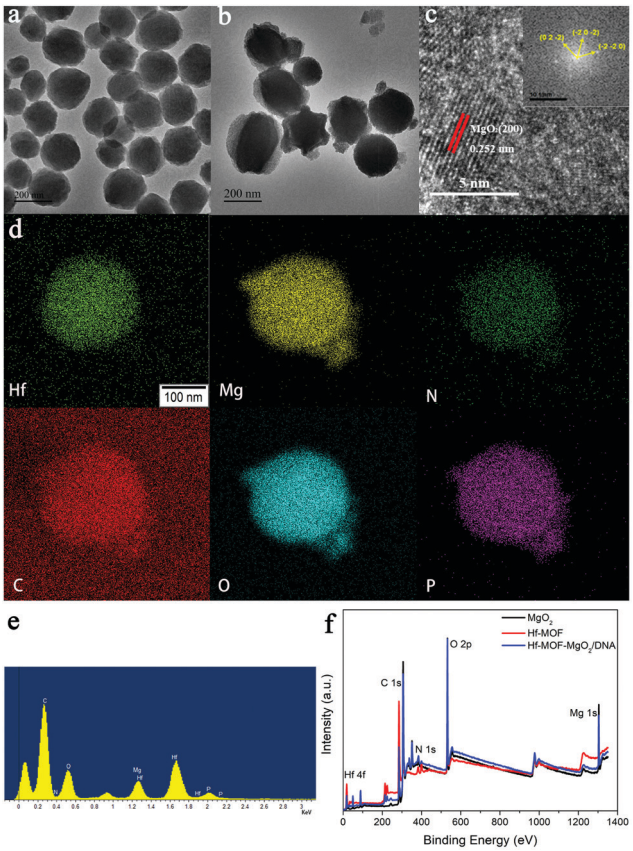

Fig. 1 Characterization of Hf-MOF and Hf-MOF-MgO_2/DNA. TEM images of the Hf-MOF (a) and Hf-MOF-MgO_2/DNA (b). (c) HR-TEM image of a single nanoparticle comprising MgO_2 nanoparticles in Hf-MOF-MgO_2/DNA. The inset is referred to a selected area showing an electron diffraction image of MgO_2. (d) Elemental mapping of Hf, Mg, O, C, N and P in Hf-MOF-MgO_2/DNA. (e) EDS of Hf-MOF-MgO_2/DNA. (f) XPS spectra of MgO_2, Hf-MOF and Hf-MOF-MgO_2/DNA.

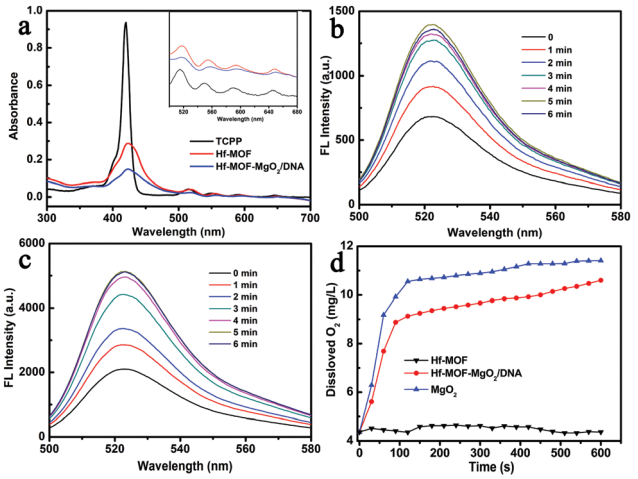

Fig. 2 (a) UV-vis absorption spectra of H_2TCPP, Hf-MOF and Hf-MOF-MgO_2/DNA. Fluorescence spectra of DCFH after incubation with the Hf-MOF (b) and Hf-MOF-MgO_2/DNA (c) under different irradiation times. (d) The dissolved O_2 content of the newly synthesized MgO_2, Hf-MOF and Hf-MOF-MgO_2/DNA dispersed in water.

PXRD patterns of Hf-MOF and Hf-MOF-MgO_2/DNA showed the characteristic peaks present in the simulated one obtained from the single-crystal data of PCN-224, confirming the stability of the Hf-MOF.

Next, we studied the photophysical properties of Hf-MOF and Hf-MOF-MgO_2/DNA in detail. H_2TCPP belongs to the porphyrin family, which showed the characteristic UV-vis absorption peaks of porphyrin at 419 nm for the Soret band and four peaks at 514, 549, 590 and 645 nm for the Q band (Fig. 2a). In comparison, Hf-MOF and Hf-MOF-MgO_2/DNA showed slight red shifts for all the bands relative to H_2TCPP, since the peaks appeared at 437, 524, 558, 597, and 652 nm. The redshift was attributed to the enlarged conjugated area of porphyrins after the formation of the Hf-MOF, which is in accordance with the reported literature.[44] Importantly, MgO_2 and DNA had no effect on the UV-vis absorption of the Hf-MOF. The fluorescent probe 2′,7′-dichlorofluorescein (DCFH) was used to investigate the ROS generation ability of Hf-MOF and Hf-MOF-MgO_2. Compared with MgO_2 and Hf-MOF, Hf-MOF-MgO_2 showed a stronger fluorescence under light irradiation, indicating the excellent ability of Hf-MOF-MgO_2 to produce ROS (Fig. S6, ESI†). In addition, in order to optimize the PDT performance of Hf-MOF-MgO_2, we measured the ROS capacity of the Hf-MOF combined with different amounts of MgO_2. The optimal ratio of Hf^{4+}/Mg^{2+} in Hf-MOF-MgO_2 determined by inductively coupled plasma (ICP) is 3 : 1, which can produce the optimal ROS amount (Fig. S6, ESI,† Hf-MOF-MgO_2-e). The UV-vis spectra of Hf-MOF-MgO_2 still showed clear Soret bands and four Q bands when the Hf-MOF reacted with different amounts of MgO (Fig. S7, ESI†). DNA was further functionalized on Hf-MOF-MgO_2-e, as confirmed by the UV-vis absorbance of DNA (Fig. S8, ESI†), forming Hf-MOF-MgO_2/DNA. The fluorescence of DCFH remarkably increased with the increasing irradiation time of light irradiation, corresponding to the increased generation ROS (Fig. 2b and c). The ability to generate ROS by Hf-MOF-MgO_2/DNA was better than that of the Hf-MOF under the same light irradiation time, confirming the significant role of MgO_2 in PDT.

The amount of oxygen generated by Hf-MOF-MgO_2/DNA was also determined. The freshly synthesized MgO_2, Hf-MOF and Hf-MOF-MgO_2/DNA were dissolved in H_2O. The concentration of dissolved oxygen was monitored in real time using a portable oxygen meter. As shown in Fig. 2d, the freshly synthesized MgO_2 and Hf-MOF-MgO_2/DNA showed a higher oxygen content in water than that of the Hf-MOF. In order to visualize the formation of oxygen bubbles, images of the visible O_2 bubbles were captured after adding the freshly synthesized MgO_2 or Hf-MOF-MgO_2/DNA in water (Fig. S9, ESI†).

The cytotoxicity of Hf-MOF-MgO_2/DNA was evaluated using a standard Cell Counting Kit-8 (CCK-8) to assess its biocompatibility. Breast cancer 4T1 cells, lung cancer A549 cells, and normal LO2 cells were incubated with Hf-MOF-MgO_2/DNA at different TCPP gradient concentrations (0, 2.5, 5, 10, 20, and 40 μg mL^{-1}) for 24 h. No obvious cytotoxicity was observed for Hf-MOF-MgO_2/DNA in our tested concentration range (Fig. 3a).

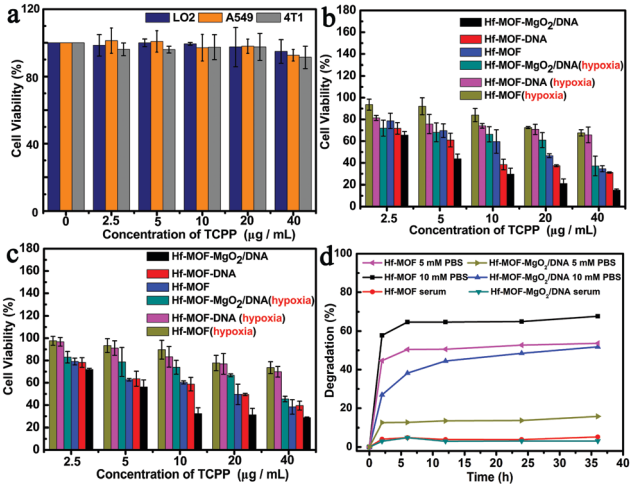

Fig. 3 (a) Cytotoxic effects of Hf-MOF-MgO_2/DNA at different concentrations for 24 h on 4T1, A549 and LO2 cells evaluated by CCK-8. Cell viability of 4T1 (b) and A549 (c) cells after incubation with Hf-MOF, Hf-MOF-DNA and Hf-MOF-MgO_2/DNA at different concentrations with light irradiation. (d) Degradation rates of Hf-MOF and Hf-MOF-MgO_2/DNA at different concentrations (5 mM PBS, 10 mM PBS and serum) after 36 h incubation.

The significance of the results obtained was also evaluated, revealing no significant difference between the tumor and normal cells treated with different concentrations of Hf-MOF-MgO_2/DNA and the same untreated cells. The above experiments demonstrated that Hf-MOF-MgO_2/DNA had good biocompatibility *in vitro*.

The viability of 4T1 and A549 cells treated with Hf-MOF, Hf-MOF-DNA and Hf-MOF-MgO_2/DNA containing different TCPP concentrations was evaluated under normoxia and hypoxia conditions (Fig. 3b and c). Under normoxia conditions, Hf-MOF-MgO_2/DNA exhibited a higher phototoxicity in both 4T1 and A549 cells under light irradiation than that of the Hf-MOF and Hf-MOF-DNA, which may be attributed to the high O_2 production of MgO_2. In addition, the viability of 4T1 cells was lower than that of A549 cells in our tested concentration range. After PDT treatment *in vitro*, the Hf-MOF-MgO_2/DNA platform functionalized by the aptamer specifically targeted 4T1 cells and achieved a survival rate of 15.15% for 4T1 cells, while the survival rate for A549 cells was 28.69% under the same conditions, indicating that Hf-MOF-MgO_2/DNA could specifically target 4T1 cells to exhibit PDT effects. Based on the targeted effect, the survival rate of 4T1 cells incubated with Hf-MOF-MgO_2/DNA or Hf-MOF-DNA was also lower than that of the Hf-MOF group. Under hypoxia conditions, Hf-MOF-MgO_2/DNA also presented excellent phototoxicity towards 4T1 cells and A549 cells. Hf-MOF-MgO_2/DNA functionalized by the aptamer specifically targeted 4T1 cells which achieved a survival rate of 37.14% for 4T1 cells, while the survival rate for A549 cells was 45.46%. Similar to normoxia conditions, Hf-MOF-MgO_2/DNA exhibited a higher phototoxicity than that of the Hf-MOF and Hf-MOF-DNA, which undoubtedly further proved that MgO_2 can alleviate tumor hypoxia of PDT. Moreover, all CCK-8 assays displayed dose dependent cell viability.[27,45] All the experiments demonstrated that Hf-MOF-MgO_2/DNA showed enhanced and targeted PDT *in vitro*. In order to evaluate the stability of the Hf-MOF, the content of TCPP ligands in PBS and the serum supernatants of Hf-MOF and Hf-MOF-MgO_2/DNA were measured to analyze the degree of degradation (Fig. S10 and S11, ESI†). As shown in Fig. 3d, Hf-MOF and Hf-MOF-MgO_2/DNA were stable in the serum. However, the Hf-MOF was unstable in PBS due to the high affinity of Hf^{4+} to phosphate ions. TCPP ligands were released rapidly in both 5 mM and 10 mM PBS. Due to the coordination interaction between MgO_2 and Hf-MOF, the stability of Hf-MOF-MgO_2/DNA in PBS was greatly improved. Therefore, because of the concentration of phosphate in blood was less than 5 mM, Hf-MOF-MgO_2/DNA can be considered in the biomedical field.

In order to verify the targeting effect of DNA on 4T1 cells, TCPP fluorescence was detected by confocal laser scanning microscopy (CLSM) imaging. As shown in Fig. 4a, 4T1 cells showed obvious TCPP red fluorescence, which was significantly higher than that of A549 cells. This result verified that Hf-MOF-MgO_2/DNA could specifically target 4T1 cells and effectively aggregate in 4T1 cells. Additionally, the PDT effect of Hf-MOF-MgO_2/DNA toward cancer cells was also studied by calcein-AM and PI double staining under normoxia and hypoxia conditions. As shown in Fig. 4b and Fig. S12–S15 (ESI†), the Hf-MOF-MgO_2/DNA group showed more dead cells, revealed by red fluorescence than that in other groups under hypoxia and normoxia conditions. The result was consistent with that obtained by CCK-8, which further emphasized the importance of MgO_2 in PDT enhancement. Therefore, the PDT effect of

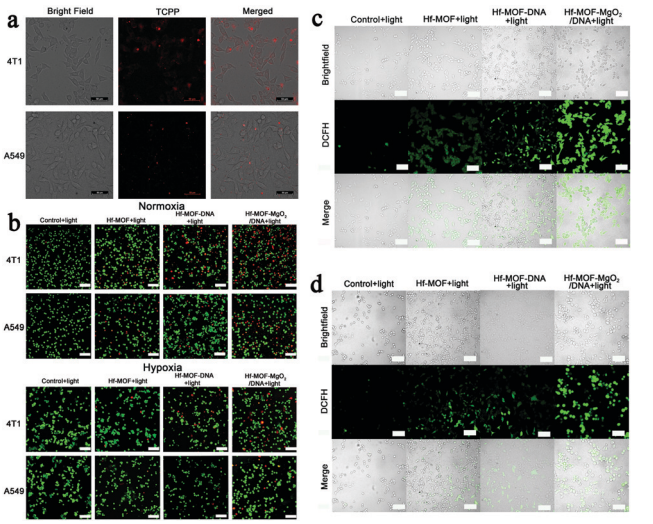

Fig. 4 (a) Confocal fluorescence images of 4T1 cells and A549 cells incubated with Hf-MOF-MgO_2/DNA for 3 h. Scale bar: 50 μm. (b) Confocal fluorescence images of calcein-AM/PI stained 4T1 cells and A549 cells after incubation with Hf-MOF, Hf-MOF-DNA and Hf-MOF-MgO_2/DNA with light irradiation (the green color represents live cells and the red color represents dead cells). Scale bar: 100 μm. Confocal fluorescence images of ROS generation in 4T1 (c) and A549 (d) cells after different treatments. Scale bar: 100 μm.

Hf-MOF-MgO_2/DNA was superior to those of Hf-MOF and Hf-MOF-DNA. Moreover, the effect was negligible in the absence of light irradiation, suggesting its excellent biocompatibility (Fig. S16, ESI†). All these results further emphasize the importance of MgO_2 and DNA in enhancing and targeting effects in PDT.

Besides, fluorescence imaging technology was used to further study the production of ROS in tumor cells mediated by Hf-MOF-MgO_2/DNA. 2′,7′-Dichlorofluorescein diacetate (DCFH-DA) is sensible to the presence of ROS, since its fluorescence is proportional to their amount; thus, it can be used to evaluate the formation of ROS in tumor cells by fluorescence microscopy (Fig. 4c and d). The blank cells and the ones treated with Hf-MOF or Hf-MOF-MgO_2/DNA in the absence of light irradiation showed almost negligible fluorescence (Fig. S17, ESI†). In contrast, Hf-MOF, Hf-MOF-DNA, and especially Hf-MOF-MgO_2/DNA treated cells in the presence of light irradiation cells showed clear fluorescence, suggesting the production of a large amount of ROS.

Based on the excellent therapeutic performance of Hf-MOF-MgO_2/DNA against tumor cells *in vitro*, the detailed toxicity *in vivo* was further investigated using mice bearing subcutaneous 4T1 tumors. Hf-MOF-MgO_2/DNA was administered intravenously for tumor treatment. As shown in Fig. S18 (ESI†), the Hf-MOF-MgO_2/DNA fluorescence signal could be observed in the tumor region after injection for 2 h. With prolonged time, Hf-MOF-MgO_2/DNA gradually aggregated to the tumor region. Due to the enhanced permeability and retention effect (EPR) and targeted therapy, the fluorescence intensity in the tumor region reached the maximum value after intravenous injection for 12 h.[30,46] To clarify the body distribution of Hf-MOF-MgO_2/DNA, the main organs as well as the tumor tissue were harvested and imaged after intravenous injection for 24 h. A stronger fluorescence intensity was observed in the tumor tissue compared with that of the liver and other organs. This result further proved the excellent targeting performance of Hf-MOF-MgO_2/DNA *in vivo*.

In tumor therapy experiments, mice were divided into 7 groups: (1) control; (2) Hf-MOF; (3) Hf-MOF-MgO_2/DNA; (4) control + light; (5) Hf-MOF + light; (6) Hf-MOF-DNA + light; and (7) Hf-MOF-MgO_2/DNA + light. Next, the relationship between the tumor volume and time in the seven groups was evaluated to determine the antitumor effect of the different treatments (Fig. 5a). The mouse group treated with Hf-MOF-MgO_2/DNA under light irradiation showed a significantly reduced tumor (Fig. 5b, c and Fig. S19, ESI†). In contrast, the tumor volume was only partially reduced in the Hf-MOF and Hf-MOF-DNA group under light irradiation group. This enhanced therapeutic effect might be due to the specific targeting of tumor cells and self-generation of O_2. Our hypothesis was that the enhanced PDT effect on the tumor after the injection of Hf-MOF-MgO_2/DNA was due to the decomposition of the decorated MgO_2 NPs resulting in the production of O_2, thus reducing tumor hypoxia. In addition, Hf-MOF and Hf-MOF-DNA showed no significant therapeutic effect without light irradiation. The body weight was continuously monitored in all mice

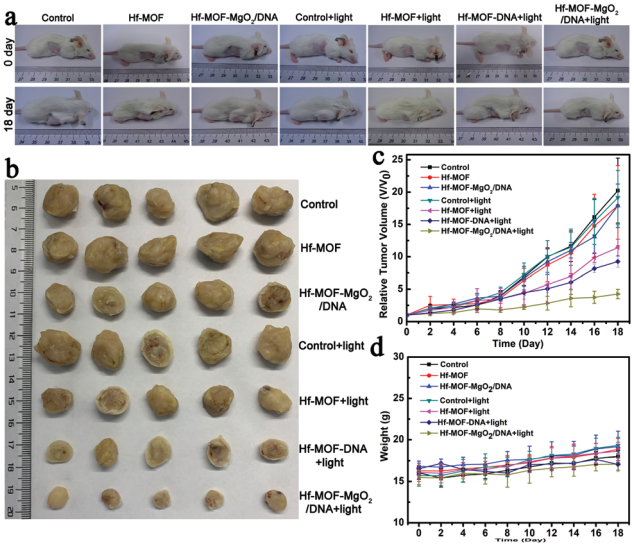

Fig. 5 *In vivo* antitumor study of Hf-MOF-MgO_2/DNA. (a) Photographs of 4T1 tumor-bearing mice before treatment and on day 18 after being subjected to various treatments. (b) Representative photographs of the collected tumors. (c) Relative tumor volume after various treatments. (d) Body weight after various treatments.

throughout the entire treatment and the results in Fig. 5d revealed no changes among the groups. This conclusion was also in good agreement with the CCK-8 assay on 4T1 cells, further indicating that the self-supplying O_2 nanosystem (Hf-MOF-MgO_2/DNA) had less dark toxicity.

The collected tumors after PDT were also used for histological analysis. The H&E staining and TUNEL staining revealed that most of the cells exhibited severe histological damage and apoptosis in the tumor of the Hf-MOF-MgO_2/DNA + light group (Fig. 6a). The expression of the hypoxia inducible factor (HIF-1α) protein as an indicator of tumor hypoxia was evaluated to further confirm the ability of Hf-MOF-MgO_2/DNA to ameliorate hypoxia in the tumor (Fig. 6b). HIF-1α fluorescence red

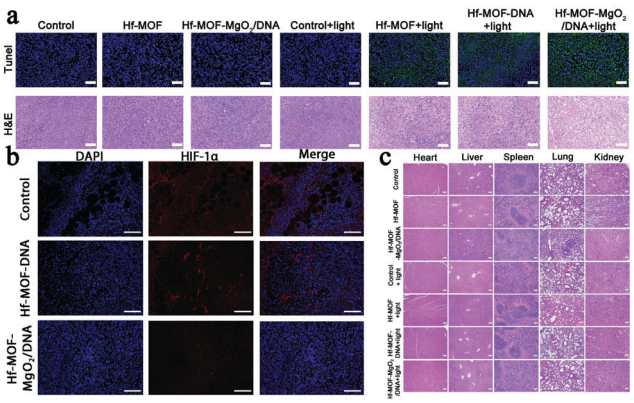

Fig. 6 PDT in a subcutaneous tumor model after treatment. (a) TUNEL staining and H&E staining of tumors with different treatments. (b) Immunofluorescence staining of HIF-1α expression. Red: HIF-1α. Blue: Nuclei stained with DAPI. (c) H&E staining images obtained from major organs after 18 days by the intravenous injection. Scale bar: 100 μm.

staining in the tumors treated with Hf-MOF-MgO_2/DNA was very weak compared with those in the tumors treated with PBS and Hf-MOF-DNA, indicating that MgO_2 could produce O_2 to reduce tumor hypoxia. In addition, the main organs of the mice after the therapy were dissected and analyzed. The morphologies of the main organs and tissues of the mice in each group were analyzed by H&E staining, showing no evident tissue damage or the presence of inflammatory factors (Fig. 6c). These results demonstrated that Hf-MOF-MgO_2/DNA possessed a strong photodynamic effect and good biocompatibility *in vivo*, with no evident toxicity.

Conclusions

In summary, a self-supplying O_2 nanosystem (Hf-MOF-MgO_2/DNA) based on magnesium peroxide nanoparticles and an aptamer functionalized Hf-MOF was constructed. This nanosystem was able to produce oxygen in sufficient quantities to reduce hypoxia and enhance the effect of PDT. The ability of the aptamer to specifically target the tumor cells enables Hf-MOF-MgO_2/DNA to perform targeted therapy. The successful results obtained *in vitro* and *in vivo* in this work indicated that Hf-MOF-MgO_2/DNA was able to provide a significantly enhanced therapeutic effect. This facile O_2 self-supplemented and aptamer functionalized MOF might provide perspectives on how to overcome hypoxia in the tumor and develop MOF-based targeted therapy.

Experimental

Materials

Hafnium(IV) tetrachloride ($HfCl_4$), 5,10,15,20-tetrakis (4-carboxyphenyl) porphyrin (H_2TCPP), magnesia (MgO) and acetic acid were purchased from Jinan Camolai Trading Company. *N*,*N*′-Dimethylformamide (DMF), absolute ethyl alcohol (C_2H_5OH), and hydrogen peroxide (H_2O_2, 30 wt%) were purchased from Sinopharm Chemical Reagent Co., Ltd. Phosphate buffer (PBS, pH = 7.4), Cell Counting Kit-8 (CCK-8), calcein-AM/PI, 2′,7′-dichlorofluorescin diacetate (DCFH-DA) and DNA sequences were purchased from Sangon Biotech Co., Ltd (Shanghai China). DMEM and trypsin–EDTA were purchased from HyClone (Logan City, USA). Penicillin–streptomycin solution was purchased from Thermo Fisher Scientific. Fetal bovine serum (FBS) was purchased from biological industries. The mouse breast cancer cell line 4T1, human lung adenocarcinoma cancer cell line A549 and normal human hepatocyte cell line LO2 were purchased from Silver Amethyst Biotech. Co. Ltd (Beijing, China). Ultrapure water was used throughout the experiment. All the other chemicals were of analytical grade and used without further purification.

Instruments

TEM images were taken using a JEM-2100 microscope (Hitachi, Japan). Powder X-ray diffraction (PXRD) experiments were recorded using a D/Max-2500 X-ray diffractometer using Cu-Kα radiation (λ = 1.5418 Å). The contents of Mg^{2+} and Hf^{4+} ions were measured by inductively coupled plasma mass spectrometry (ICP–MS, 8900, Agilent, USA). X-ray photoelectron spectroscopy (XPS) spectra were analyzed using a Thermo Fisher Scientific ESCALAB 250Xi Spectrometer. Ultraviolet-visible (UV-vis) spectra were recorded using a Cary 60 UV/vis spectrophotometer (Agilent). The fluorescence measurements were recorded using an F-4600 flow meter (Hitachi, Japan). ROS were measured under 650 nm light irradiation at a low power density of 0.28 W cm^2. CCK-8 assay was performed using a microplate reader (EP0CH2, China). Confocal fluorescence imaging was performed using a Leica TCS SP8 inverted confocal microscope (Leica, Germany) with an objective lens (×20). *In vivo* imaging was performed using the IVIS Lumina LT imaging system. The DNA sequence was ACC-GAC-CGT-GCT-GGA-CTC-TAC-ATA-GTC-CTC-ACT-CTA-AAC-GAT-GGT-CCC-TAG-TAT-GAG-CGA-GCG-TTG-CG.

Synthesis of the Hf-MOF

$HfCl_4$ (4 mg, 0.0125 mmol), H_2TCPP (10 mg, 0.0126 mmol), 0.4 mL of acetic acid and 8 mL of DMF were mixed in a three-neck flask. After stirring for 10 min at room temperature, the mixture was kept in an oil bath at 80 °C for 2 h. After cooling, 6 mL of DMF was added to the round bottom flask and the reaction was continued for 24 h. At the end of the reaction, dark purple solid products were collected by centrifugation, followed by washing with fresh DMF three times. Finally, the Hf-MOF was dried under vacuum at 60 °C.

Synthesis of Hf-MOF-MgO_2 and functionalization with DNA

4 mg of the as-prepared Hf-MOF was dispersed in 4 mL of ethanol with 0.5 mg (a), 1.0 mg (b), 1.5 mg (c), 2.0 mg (d), and 2.5 mg (e) nanoscale MgO. After 10 min of ultrasonication, 4 mL of H_2O_2 (30 wt%) was poured into the above mixed solution. After stirring for 4 h, the solid part was separated from the suspension. Subsequently, the products were collected by centrifugation, followed by washing with ethanol. Finally, different complex quantities of Hf-MOF-MgO_2 were obtained.

Hf-MOF-MgO_2 functionalization by DNA (Hf-MOF-MgO_2/DNA) was performed as follows: Hf-MOF-MgO_2 was added into 500 μL of DNA (1 OD) and gently shaken overnight. The nanoparticles were centrifuged to remove the free DNA and washed with water three times.

The ROS generation ability of Hf-MOF and Hf-MOF-MgO_2/DNA

The ROS generation measurement *in vitro* was carried out using 2′,7′-dichlorofluorescein (DCFH) as a probe. 5.0 mg of DCFH-DA was dissolved in 10.0 mL of DMSO to obtain 1.03 mM DCFH-DA. In order to hydrolyze DCFH-DA to DCFH, 0.5 mL of 1.03 mM DCFH-DA was added to 2.0 mL of 10 mM sodium hydroxide and reacted for 30 minutes at room temperature without irradiation. The hydrolysis reaction was stopped by adding 10 mL of PBS (pH = 7.4). Before use, the DCFH solution was kept on ice away from light.

Hf-MOF or Hf-MOF-MgO_2/DNA nanoparticles were mixed with the DCFH stock. Then, the mixture was irradiated with

650 nm light irradiation. The solution was centrifuged immediately after 1 min of each irradiation and the fluorescence of the supernatant was measured to estimate the ROS produced.

Quantitative analysis of the degradation rate of Hf-MOF and Hf-MOF-MgO_2/DNA

First, the standard curve of TCPP absorbance and concentration is plotted. This is done by configuring a range of concentrations of TCPP (0.1, 0.5, 1,2, 5 and 10 μM) standard solutions. Furthermore, the absorbance value at 418 nm was analyzed and recorded. Next, 1 M NaOH was used to digest Hf-MOF and Hf-MOF-MgO_2/DNA to determine the content of TCPP. Hf-MOF and Hf-MOF-MgO_2/DNA containing the same concentration of TCPP were dispersed in 5 mM PBS buffer, 10 mM PBS buffer and bovine serum, respectively. The supernatant was collected after the incubation time reached 2, 6, 12, 24 and 36 h, respectively; the content of TCPP in the supernatant was recorded, and the degradation rate was calculated.

Cell culture

4T1, A549 and LO2 cells were cultured in the DMEM supplemented with 10% FBS and 1% penicillin–streptomycin (10 000 U mL^{-1}). All cells were incubated at 37 °C in a humidified atmosphere containing 5% CO_2. When the cells were grown to about 80%, the culture medium was aspirated and the cells were rinsed once with PBS (0.01 M, pH 7.4). Then, 1 mL of trypsin–EDTA (0.25%) was added to the culture dish to digest the cells for 1–2 min. The cells were collected by centrifugation (800 r min^{-1}, 3 min) and cultured in a particular dish for cell culture for subsequent cell viability determination and cell imaging.

Cellular uptake

To evaluate the specific cell targeting ability of Hf-MOF-MgO_2/DNA, 4T1 and A549 cells were seeded in confocal dishes at a density of 1×10^5 cells per well. Subsequently, the cells were incubated with Hf-MOF-MgO_2/DNA (40 μg mL^{-1} TCPP) for 3 h. After washing with 1 × PBS (0.01 M) three times, the cells were finally imaged by CLSM.

Cell compatibility

4T1, A549 and LO2 cells were carefully seeded in 96-well microplates at a density of 1×10^4 cells in 100 μL culture medium each well and incubated for 12 h. Subsequently, the cells were treated with different concentrations (0, 2.5, 5, 10, 20, and 40 μg mL^{-1} TCPP) of Hf-MOF-MgO_2/DNA for 24 h. Then, 10 μL CCK-8 was added to each well, and the absorbance of each well at 450 nm was measured using a microplate reader. The cell viability was evaluated according to the equation: cell viability (%) = $(A_{test} - A_0/A_{control} - A_0) \times 100\%$. In the formula, "$A_{test}$, A_0, and $A_{control}$" represent the absorbance of experimental wells with cells and nanoparticles, blank wells without nanoparticles and cells, and control wells with cells but without nanoparticles, respectively.

Cell phototoxicity

4T1 and A549 cells were seeded in 96-well microplates at a density of 1×10^4 cells in 100 μL DMEM each well and incubated for 12 h. The culture medium was replaced by the fresh medium containing Hf-MOF, Hf-MOF-DNA or Hf-MOF-MgO_2/DNA at TCPP concentrations of 0, 2.5, 5, 10, 20, and 40 μg mL^{-1}. After 3 h, the cells were irradiated with 650 nm light irradiation for 6 min and further incubation for 24 h. Finally, the cell viability was evaluated using the CCK-8 assay kit. The hypoxia conditions were constructed according to a reported method.[30] 96-well plates were placed inside of a transparent box, evacuated for 30 min and flushed into nitrogen for 1 h. Then, the 96-well plates were sealed with parafilm and light irradiation.

Intracellular ROS generation

4T1 and A549 cells were seeded in 1 mL of DMEM with 1×10^5 cells in the CLSM-exclusive culture disk and incubated for 12 h. Later, the culture medium was replaced with Hf-MOF, Hf-MOF-DNA, and Hf-MOF-MgO_2/DNA (40 μg mL^{-1} TCPP) and incubated for another 3 h at 37 °C. Then, the cells were washed with PBS and co-incubated with DCFH-DA at 37 °C for 20 min. After this, the cells were washed with serum-free cell culture medium to fully remove DCFH-DA that did not enter the cells and cells in the light group were irradiated with 650 nm light irradiation for 6 min. Finally, intracellular ROS generation was observed under a CLSM (E_x = 488 nm and E_m = 525 nm).

Confocal images of calcein AM and PI co-stained tumor cells

4T1 and A549 cells were added to 2 mL of DMEM with a cell concentration of 1×10^5 cells per mL^{-1} and incubated overnight in a six-well culture plate. Then, the cells were treated with (1) control; (2) Hf-MOF; (3) Hf-MOF-MgO_2/DNA; (4) control + light; (5) Hf-MOF + light; (6) Hf-MOF-DNA + light; (7) Hf-MOF-MgO_2/DNA + light, respectively, followed by another 24 h of incubation. The cells were digested with trypsin–EDTA and added into cell suspension. The cell suspension was centrifuged (1000 r min^{-1}, 3 min) to remove the supernatant and washed several times with PBS buffer. The above treated cells were incubated with 1 mL of calcein AM/PI for 20 min. Subsequently, the fluorescence images of the stained cells were obtained using a CLSM. The hypoxia conditions were constructed according to the following methods: six-well plates were placed inside of a transparent box, evacuated for 30 min and flushed into nitrogen for 1 h. Then, the six-well plates were sealed with parafilm and light irradiation.

Animal model

All animal experiments were conducted in accordance with the institutional animal care guidelines, approved by the Institutional Animal Care and Use Committee of Linyi University. Female Balb/c mice (20–25 g) were purchased from Beijing Charles River Laboratory Animal Technology Co., Ltd. (China). All animal experiments were conducted in accordance with the guidelines and regulations for the use and care of animals. The

tumor model was established by the subcutaneous injection of 1×10^6 4T1 cells suspended in 100 μL PBS into the right axilla of the mice. Tumors were allowed to grow for 5–7 days before use.

Therapeutic effect *in vivo*

When the tumor volumes reached approximately 100 mm^3, tumor bearing mice were randomly divided into seven groups (n = 5 mice per group) treated with different formulations: (1) control; (2) Hf-MOF; (3) Hf-MOF-MgO_2/DNA; (4) control + light; (5) Hf-MOF + light; (6) Hf-MOF-DNA + light; (7) Hf-MOF-MgO_2/DNA + light. Then, mice were intravenously treated with Hf-MOF, Hf-MOF-DNA or Hf-MOF-MgO_2/DNA (100 μL, 1 mg mL^{-1}). Mice in the light group received 650 nm light irradiation for 6 min after the intravenous injection for 12 h. The tumor volume and body weight were measured every two days using a digital caliper, and the volumes (V) were calculated using the equation: $V = 0.5 \times (\text{length}) \times (\text{width})^2$. The relative tumor volume (V/V_0) represented changes of tumor volumes, where V_0 is the tumor volume at the beginning of treatment.

In vivo imaging

The tumor model was established by subcutaneously injecting 4T1 cells into the right leg of mice. After the tumor volume reached 100 mm^3 around, the mice were intravenously treated with Hf-MOF-MgO_2/DNA for imaging studies. At the scheduled time after injection, the tumor imaging was carried out *via* the IVIS Lumina LT imaging system.

Histological analysis

Eighteen days later, all of the mice were sacrificed and major organs (including heart, liver, spleen, lungs, kidneys and tumors) were harvested and fixed in paraformaldehyde (4%), dehydrated, embedded in paraffin, sectioned and stained with H&E (hematoxylin and eosin staining assay). The harvested tumors were also stained with TUNEL (terminal deoxynucleotidyl transferase-mediated dUTP-biotin nick end labeling) to further study the apoptosis of tumor cells.

Hypoxia study *in vivo*

4T1 tumor-bearing mice were randomly divided into three groups, and accepted the injections as described below: PBS, Hf-MOF-DNA, and Hf-MOF-MgO_2/DNA (1 mg mL^{-1}). After 24 h, all mice were sacrificed and the tumor tissues were collected and sectioned for HIF-1α staining.

Author contributions

The authors declare no competing financial interest.

Conflicts of interest

There are no conflicts to declare.

Acknowledgements

This work was supported by the National Natural Science Foundation of China (Grant No. 21775062, 21775063 and 22076073) and the Natural Science Foundation of Shandong Province (No. ZR2017LB019).

Notes and references

1 A. Escudero, C. Carrillo-Carrión, M. C. Castillejos, E. Romero-Ben, C. Rosales-Barrios and N. Khiar, Photodynamic therapy: photosensitizers and nanostructures, *Mater. Chem. Front.*, 2021, **5**, 3788–3812.
2 Y. T. Fan, T. J. Zhou, P. F. Cui, Y. J. He, X. Chang, L. Xing and H. L. Jiang, Modulation of Intracellular Oxygen Pressure by Dual-Drug Nanoparticles to Enhance Photodynamic Therapy, *Adv. Funct. Mater.*, 2019, **29**, 1806708.
3 T. Shen, X. Hu, Y. Liu, Y. Zhang, K. Chen, S. Xie, G. Ke, G. Song and X. B. Zhang, Specific Core-Satellite Nanocarriers for Enhanced Intracellular ROS Generation and Synergistic Photodynamic Therapy, *ACS Appl. Mater. Interfaces*, 2020, **12**, 5403–5412.
4 M. Lismont, L. Dreesen and S. Wuttke, Metal–Organic Framework Nanoparticles in Photodynamic Therapy: current Status and Perspectives, *Adv. Funct. Mater.*, 2017, **27**, 1606314.
5 J. Zhao, L. Duan, A. Wang, J. Fei and J. Li, Insight into the efficiency of oxygen introduced photodynamic therapy (PDT) and deep PDT against cancers with various assembled nanocarriers, *Wiley Interdiscip. Rev.: Nanomed. Nanobiotechnol.*, 2020, **12**, 1583.
6 A. P. Castano, T. N. Demidova and M. R. Hamblin, Mechanisms in photodynamic therapy: part two—cellular signaling, cell metabolism and modes of cell death, *Photodiagn. Photodyn. Ther.*, 2005, **2**, 1–23.
7 P. Mroz, A. Yaroslavsky, G. B. Kharkwal and M. R. Hamblin, Cell death pathways in photodynamic therapy of cancer, *Cancers*, 2011, **3**, 2516–2539.
8 C. A. Robertson, D. H. Evans and H. Abrahamse, Photodynamic therapy (PDT): a short review on cellular mechanisms and cancer research applications for PDT, *J. Photochem. Photobiol., B*, 2009, **96**, 1–8.
9 D. Wang, H. Wu, W. Q. Lim, S. Z. F. Phua, P. Xu, Q. Chen, Z. Guo and Y. Zhao, A Mesoporous Nanoenzyme Derived from Metal-Organic Frameworks with Endogenous Oxygen Generation to Alleviate Tumor Hypoxia for Significantly Enhanced Photodynamic Therapy, *Adv. Mater.*, 2019, **31**, 1901893.
10 D. W. Felsher, Cancer revoked: oncogenes as therapeutic targets, *Nat. Rev. Cancer*, 2003, **3**, 375–380.
11 A. Master, M. Livingston and A. Sen Gupta, Photodynamic nanomedicine in the treatment of solid tumors: perspectives and challenges, *J. Controlled Release*, 2013, **168**, 88–102.
12 P. Agostinis, K. Berg, K. A. Cengel, T. H. Foster, A. W. Girotti, S. O. Gollnick, S. M. Hahn, M. R. Hamblin, A. Juzeniene,

D. Kessel, M. Korbelik, J. Moan, P. Mroz, D. Nowis, J. Piette, B. C. Wilson and J. Golab, Photodynamic therapy of cancer: an update, *Ca-Cancer J. Clin.*, 2011, **61**, 250–281.

13 S. Verma, G. M. Watt, Z. Mai and T. Hasan, Strategies for enhanced photodynamic therapy effects, *Photochem. Photobiol.*, 2007, **83**, 996–1005.

14 L. Shi, F. Hu, Y. Duan, W. Wu, J. Dong, X. Meng, X. Zhu and B. Liu, Hybrid Nanospheres to Overcome Hypoxia and Intrinsic Oxidative Resistance for Enhanced Photodynamic Therapy, *ACS Nano*, 2020, **14**, 2183–2190.

15 W. Sun, L. Luo, Y. Feng, Y. Cai, Y. Zhuang, R. J. Xie, X. Chen and H. Chen, Aggregation-Induced Emission Gold Clustoluminogens for Enhanced Low-Dose X-ray-Induced Photodynamic Therapy, *Angew. Chem., Int. Ed.*, 2020, **59**, 9914–9921.

16 Y. Su, S. Lu, P. Gao, M. Zheng and Z. Xie, BODIPY@carbon dot nanocomposites for enhanced photodynamic activity, *Mater. Chem. Front.*, 2019, **3**, 1747–1753.

17 A. B. Ormond and H. S. Freeman, Dye Sensitizers for Photodynamic Therapy, *Materials*, 2013, **6**, 817–840.

18 Y. Li, J. Chu, D. Wang, L. Zhu and D. Kong, DNA nanolantern as biocompatible drug carrier for simple preparation of a porphyrin/G-quadruplex nanocomposite photosensitizer with high photodynamic efficacy, *Mater. Chem. Front.*, 2021, **5**, 3139–3148.

19 K. Lu, C. He and W. Lin, Nanoscale metal–organic framework for highly effective photodynamic therapy of resistant head and neck cancer, *J. Am. Chem. Soc.*, 2014, **136**, 16712–16715.

20 G. Lan, K. Ni and W. Lin, Nanoscale Metal–Organic Frameworks for Phototherapy of Cancer, *Coord. Chem. Rev.*, 2019, **379**, 65–81.

21 Z. Bao, K. Li, P. Hou, R. Xiao, Y. Yuan and Z. Sun, Nanoscale metal–organic framework composites for phototherapy and synergistic therapy of cancer, *Mater. Chem. Front.*, 2021, **5**, 1632–1654.

22 M. R. Younis, C. Wang, R. An, S. Wang, M. A. Younis, Z. Q. Li, Y. Wang, A. Ihsan, D. Ye and X. H. Xia, Low Power Single Laser Activated Synergistic Cancer Phototherapy Using Photosensitizer Functionalized Dual Plasmonic Photothermal Nanoagents, *ACS Nano*, 2019, **13**, 2544–2557.

23 C. Qian, J. Yu, Y. Chen, Q. Hu, X. Xiao, W. Sun, C. Wang, P. Feng, Q. D. Shen and Z. Gu, Light-Activated Hypoxia-Responsive Nanocarriers for Enhanced Anticancer Therapy, *Adv. Mater.*, 2016, **28**, 3313–3320.

24 X. Tong, A. Srivatsan, O. Jacobson, Y. Wang, Z. Wang, X. Yang, G. Niu, D. O. Kiesewetter, H. Zheng and X. Chen, Monitoring Tumor Hypoxia Using ^{18}F-FMISO PET and Pharmacokinetics Modeling after Photodynamic Therapy, *Sci. Rep.*, 2016, **6**, 31551.

25 H. Wang, D. Yu, J. Fang, C. Cao, Z. Liu, J. Ren and X. Qu, Renal-Clearable Porphyrinic Metal–Organic Framework Nanodots for Enhanced Photodynamic Therapy, *ACS Nano*, 2019, **13**, 9206–9217.

26 B. R. Xie, Y. Yu, X. H. Liu, J. Y. Zeng, M. Z. Zou, C. X. Li, X. Zeng and X. Z. Zhang, A near infrared ratiometric platform based pi-extended porphyrin metal-organic framework for O_2 imaging and cancer therapy, *Biomaterials*, 2021, **272**, 120782.

27 Y. Zhang, F. Wang, C. Liu, Z. Wang, L. Kang, Y. Huang, K. Dong, J. Ren and X. Qu, Nanozyme Decorated Metal–Organic Frameworks for Enhanced Photodynamic Therapy, *ACS Nano*, 2018, **12**, 651–661.

28 H. Min, J. Wang, Y. Qi, Y. Zhang, X. Han, Y. Xu, J. Xu, Y. Li, L. Chen, K. Cheng, G. Liu, N. Yang, Y. Li and G. Nie, Biomimetic Metal–Organic Framework Nanoparticles for Cooperative Combination of Antiangiogenesis and Photodynamic Therapy for Enhanced Efficacy, *Adv. Mater.*, 2019, **31**, 1808200.

29 Z. Gao, Y. Li, Y. Zhang, K. Cheng, P. An, F. Chen, J. Chen, C. You, Q. Zhu and B. Sun, Biomimetic Platinum Nanozyme Immobilized on 2D Metal-Organic Frameworks for Mitochondrion-Targeting and Oxygen Self-Supply Photodynamic Therapy, *ACS Appl. Mater. Interfaces*, 2020, **12**, 1963–1972.

30 C. Liu, J. Xing, O. U. Akakuru, L. Luo, S. Sun, R. Zou, Z. Yu, Q. Fang and A. Wu, Nanozymes-Engineered Metal–Organic Frameworks for Catalytic Cascades-Enhanced Synergistic Cancer Therapy, *Nano Lett.*, 2019, **19**, 5674–5682.

31 Z. M. Tang, Y. Y. Liu, D. L. Ni, J. J. Zhou, M. Zhang, P. R. Zhao, B. Lv, H. Wang, D. Y. Jin and W. B. Bu, Biodegradable Nanoprodrugs: ''delivering'' ROS to Cancer Cells for Molecular Dynamic Therapy, *Adv. Mater.*, 2020, **32**, 1904011.

32 Z. Peng, C. Wang, C. Liu, H. Xu, Y. Wang, Y. Liu, Y. Hu, J. Li, Y. Jin, C. Jiang, L. Liu, J. Guo and L. Zhu, 3D printed polycaprolactone/beta-tricalcium phosphate/magnesium peroxide oxygen releasing scaffold enhances osteogenesis and implanted BMSCs survival in repairing the large bone defect, *J. Mater. Chem. B*, 2021, **9**, 5698–5710.

33 F. Gholami, H. Mosmeri, M. Shavandi, S. M. M. Dastgheib and M. A. Amoozegar, Application of encapsulated magnesium peroxide (MgO_2) nanoparticles in permeable reactive barrier (PRB) for naphthalene and toluene bioremediation from groundwater, *Sci. Total Environ.*, 2019, **655**, 633–640.

34 S.-Y. Li, W.-X. Qiu, H. Cheng, F. Gao, F.-Y. Cao and X.-Z. Zhang, A Versatile Plasma Membrane Engineered Cell Vehicle for Contact-Cell-Enhanced Photodynamic Therapy, *Adv. Funct. Mater.*, 2017, **27**, 1604916.

35 J. Liu, H. Liang, M. Li, Z. Luo, J. Zhang, X. Guo and K. Cai, Tumor acidity activating multifunctional nanoplatform for NIR-mediated multiple enhanced photodynamic and photothermal tumor therapy, *Biomaterials*, 2018, **157**, 107–124.

36 J. J. Lin, J. S. Chen, S. J. Huang, J. H. Ko, Y. M. Wang, T. L. Chen and L. F. Wang, Folic acid-Pluronic F127 magnetic nanoparticle clusters for combined targeting, diagnosis, and therapy applications, *Biomaterials*, 2009, **30**, 5114–5124.

37 Y. Kang, W. Sun, S. Li, M. Li, J. Fan, J. Du, X. J. Liang and X. Peng, Oligo Hyaluronan-Coated Silica/Hydroxyapatite Degradable Nanoparticles for Targeted Cancer Treatment, *Adv. Sci.*, 2019, **6**, 1900716.

38 K. Kim, S. Lee, E. Jin, L. Palanikumar, J. H. Lee, J. C. Kim, J. S. Nam, B. Jana, T. H. Kwon, S. K. Kwak, W. Choe and J. H. Ryu, MOF x Biopolymer: collaborative Combination of Metal-Organic Framework and Biopolymer for Advanced Anticancer Therapy, *ACS Appl. Mater. Interfaces*, 2019, **11**, 27512–27520.

39 S. I. Hori, A. Herrera, J. J. Rossi and J. Zhou, Current Advances in Aptamers for Cancer Diagnosis and Therapy, *Cancers*, 2018, **10**, 9.

40 H. Cheng, R. R. Zheng, G. L. Fan, J. H. Fan, L. P. Zhao, X. Y. Jiang, B. Yang, X. Y. Yu, S. Y. Li and X. Z. Zhang, Mitochondria and plasma membrane dual-targeted chimeric peptide for single-agent synergistic photodynamic therapy, *Biomaterials*, 2019, **188**, 1–11.

41 L. Lang and Y. Teng, Fibroblast Growth Factor Receptor 4 Targeting in Cancer: new Insights into Mechanisms and Therapeutic Strategies, *Cells*, 2019, **8**, 31.

42 D. Wu, Y. Bai, W. Wang, H. Xia, F. Tan, S. Zhang, B. Su, X. Wang, X. Qiao and P. K. Wong, Highly pure MgO_2 nanoparticles as robust solid oxidant for enhanced Fenton-like degradation of organic contaminants, *J. Hazard. Mater.*, 2019, **374**, 319–328.

43 S. Gao, Y. Jin, K. Ge, Z. Li, H. Liu, X. Dai, Y. Zhang, S. Chen, X. Liang and J. Zhang, Self-Supply of O_2 and H_2O_2 by a Nanocatalytic Medicine to Enhance Combined Chemo/Chemodynamic Therapy, *Adv. Sci.*, 2019, **6**, 1902137.

44 J. Liu, Y. Yang, W. Zhu, X. Yi, Z. Dong, X. Xu, M. Chen, K. Yang, G. Lu, L. Jiang and Z. Liu, Nanoscale metal-organic frameworks for combined photodynamic & radiation therapy in cancer treatment, *Biomaterials*, 2016, **97**, 1–9.

45 Y. Yang, D. Zhu, Y. Liu, B. Jiang, W. Jiang, X. Yan and K. Fan, Platinum-carbon-integrated nanozymes for enhanced tumor photodynamic and photothermal therapy, *Nanoscale*, 2020, **12**, 13548–13557.

46 X.-S. Wang, J.-Y. Zeng, M.-K. Zhang, X. Zeng and X.-Z. Zhang, A Versatile Pt-Based Core–Shell Nanoplatform as a Nanofactory for Enhanced Tumor Therapy, *Adv. Funct. Mater.*, 2018, **28**, 1801783.